



Tuning the antimicrobial efficacy of nano-Ca(OH)₂ against *E. coli* using molarity

Harish¹, Pushpendra Kumar^{1,*} , Sapna Kumari², Mousumi Debnath², Amena Salim³, Rahul Singhal³, Rajendra P. Joshi⁴, and Anoop Kumar Mukhopadhyay^{1,5,*}

¹Department of Physics, Manipal University Jaipur, Jaipur, Rajasthan 303007, India

²Department of Bioscience, Manipal University Jaipur, Jaipur, Rajasthan 303007, India

³Department of Physics, Malaviya National Institute of Technology, Jaipur 302017, India

⁴RI Instruments and Innovation India, Haldwani, Uttarakhand 263139, India

⁵Department of Physics, Biyani Girls College, Vidhyadhar Nagar, Jaipur, Rajasthan 302039, India

Received: 11 December 2021

Accepted: 4 April 2022

© The Author(s), under exclusive licence to Springer Science+Business Media, LLC, part of Springer Nature 2022

ABSTRACT

The present work reports on tuning the antimicrobial efficacy of nano-Ca(OH)₂ against *E. coli* by appropriately tuning the molarity of the reactants. Thus, the phase pure nano-Ca(OH)₂ powders are developed by an inexpensive chemical precipitation technique using equimolar concentrations (e.g., 0.4, 0.6, 0.8, and 1 M) of [Ca(NO₃)₂·4H₂O] and NaOH solutions. The characterizations by the XRD, FESEM, TEM, FTIR, DTA, TGA, UV–Vis spectroscopy, and agar plate well diffusion methods show that the higher the molarity of reactants, the higher the nanocrystallite size, the lower the optical band gap energy and the higher the (%) increase in inhibition zone diameters (*D*_{iz}) for exposure periods in the range of 6–48 h. These results are discussed in terms of relative variations in the microstructure, lattice strain, thermal stability, optical band gap energy, defect structure, and the amount of (OH[−]) ions. Further, the possible mechanisms of antimicrobial behavior are suggested. Finally, the implications of these results in terms of microstructurally tuned nano-Ca(OH)₂ materials development for prospective futuristic applications are highlighted.

Introduction

Calcium hydroxide [Ca(OH)₂] is an age-old material [1]. However, it is also an ever-evolving material [1–19]. It possesses a myriad of excellent properties. It is biocompatible. It also has antibacterial,

antimicrobial, and antifungal properties as well as controllable chemical reactivity. It can also store thermal energy due to high enthalpy. It has reasonable mechanical properties to act as good filler material. Therefore, these properties attract many researchers for various applications of it. The

Handling Editor: Annela M. Seddon.

Address correspondence to E-mail: pushpendra.kumar@jaipur.manipal.edu; mukhopadhyay.anoop@gmail.com

<https://doi.org/10.1007/s10853-022-07198-5>

Published online: 22 April 2022

following discussion, therefore, tries to give an overview of the correlation between different applications of $\text{Ca}(\text{OH})_2$ with the relevant properties.

Because of its intrinsic antibacterial properties, a major application area of calcium hydroxide is in dentistry and endodontics. The particle size of $\text{Ca}(\text{OH})_2$ is about 80–500 nm for commercial material used in endodontic applications [1]. On the other hand, calcium hydroxide is also being applied in conjunction with photo-bio-modulation to study the apexogenesis of immature permanent teeth in dog model [2], thereby highlighting its huge biocompatibility and diverse applicability. In recent work, $\text{Ca}(\text{OH})_2$ and photo-assisted oral disinfection have been applied in the indirect pulp treatment of young permanent molars and found to be equally effective [3] that further highlights the importance of $\text{Ca}(\text{OH})_2$ in antibacterial activity. Thus, it is not surprising at all to note that very recent work focuses on the comparison of the antibacterial efficacy of Tea tree oil, Nisin, and $\text{Ca}(\text{OH})_2$ of unknown particle size against *Enterococcus faecalis*, a well-known bacterium [4]. Unfortunately, however, the particle size is not always mentioned [2–4]. Similar work on the antibacterial efficacy of $\text{Ag}/\text{Ca}(\text{OH})_2$ nanoparticles of 30 nm size has been reported by other researchers [5].

Similar philosophy identifies an innovative use of calcium hydroxide for live-stock sanitization purposes [6]. Here, however, the particle size of $\text{Ca}(\text{OH})_2$ is about 1–3 mm [6]. Thus, along with dental applications, both biocompatibility, and antibacterial characteristics promote the application of $\text{Ca}(\text{OH})_2$ in emerging areas such as advanced bone restoration [7]. Here again, the particle size is not specifically mentioned. A combination of reasonable mechanical properties and biocompatibility promotes its recent application in food packaging film [8] where it also acts as an adsorbent of CO_2 . In this case, the particle size is about 10 μm .

Because of its high enthalpy, another important area of application for calcium hydroxide emerges as thermochemical energy storage [9]. Here, the particle size is about 5–30 μm . A novel composite of $\text{CaO}/\text{Ca}(\text{OH})_2$ on a SiC/Si ceramic honeycomb support has been very recently employed to enhance the efficacy of thermochemical energy storage [10]. This research involves 20–200 nm particle size of $\text{Ca}(\text{OH})_2$.

As a material, $\text{Ca}(\text{OH})_2$ is also very important for the cement industry. Therefore, recent research also emphasizes how the presence of calcium hydroxide

modifies the alkali-silica reaction of alkali-activated slag mortars activated by sodium hydroxide [11]. A larger particle size of 1–50 μm is involved in this work. Considering its importance in the cement industry, a lot of current focus is directed on the study of the mechanical and fracture properties in a calcium silicate hydrate and calcium hydroxide composite using reactive molecular dynamics simulation [12]. It is also being utilized for portland cement production and hardening [13, 14]. It involves about 83 nm particle size of $\text{Ca}(\text{OH})_2$ [13].

A major emerging application area of $\text{Ca}(\text{OH})_2$ is in the domain of cultural heritage restoration. It happens because it can easily react with nitrates, sulfates, phosphates, etc. It is thus used in stone conservation [15], for consolidation of dolostone in historical buildings [16], and cultural heritage conservation [17]. The ability of $\text{Ca}(\text{OH})_2$ to react with phosphates has been very recently utilized for the removal of phosphates from fertilizers used in the soil [18]. The stone conservation involves $\text{Ca}(\text{OH})_2$ particle size of about 90–100 nm [15]. In dolostone consolidation, however, the particle size is much larger, e.g., 0.5–3 μm [16]. A very recent effort involves the usage of $\text{Ca}(\text{OH})_2$ and $\text{Se-Ca}(\text{OH})_2$ nanocomposites for enhancing the seed priming effect in *Vigna radiata* mung bean grams [19]. The aforesaid discussion of literature information confirms that different applications of $\text{Ca}(\text{OH})_2$ and/or $\text{Ca}(\text{OH})_2$ based composites involve drastically different particle size with a range of as wide as, e.g., 20 nm–3 mm [1–19]. There is no doubt that nanometer size particle will have large surface area and hence high chemical reactivity on the surface which is so much needed for antibacterial applications. This is where the scope emerges for the present study. Despite such a huge variety of application possibilities, the systematic studies on how a change of molarity of chemical reactants in the chemical precipitation process affects the physical and especially, the antimicrobial efficacy of calcium hydroxide are far from well studied, if at all [1–19]. This is where the focused scope of the present study becomes concentrated as an objective.

On the other hand, only a handful of related studies reported for a wide variety of materials, per se, indicate that microstructural parameters and hence, the physical as well as antimicrobial properties may be affected [20–22] due to changes in molarity. This lack of knowledge base in the case of calcium hydroxide frames the further definitive scope

of the present work. Thus, the objective of the present work is to tune the antimicrobial efficacy of nano- Ca(OH)_2 against a Gram-negative *Escherichia coli* (*E. coli*) bacteria by simultaneous molarity change of calcium nitrate tetrahydrate [$\text{Ca(NO}_3)_2 \cdot 4\text{H}_2\text{O}$] and sodium hydroxide (NaOH). The details of material synthesis, characterization, and antimicrobial efficacy study techniques are already reported by us elsewhere [23, 24] and hence will be only briefly described here.

Experimental details

Materials and methods

In the present work, calcium hydroxide [Ca(OH)_2] powders S1, S2, S3, and S4 were synthesized by the well-known chemical precipitation method using equimolar aqueous (e.g., 0.4, 0.6, 0.8, and 1.0 M) calcium nitrate tetrahydrate [$\text{Ca(NO}_3)_2 \cdot 4\text{H}_2\text{O}$] (AR grade, 99.99% pure, Merck, Bengaluru, India) and sodium hydroxide (NaOH) (AR grade, 99.99% pure, Bengaluru, India) solutions. As mentioned earlier, further details are given elsewhere [23, 24]. The structural phase analysis, crystallite size estimation, and strain evaluation for all the samples were done by using the XRD technique (X'pert pro MPD diffractometer, PANalytical, Almelo, Netherlands; 40 kV and 30 mA, CuK_α monochromatic radiation of $\lambda = 1.5406 \text{ \AA}$) following the well-known Debye–Scherrer and Williamson–Hall plot techniques [25, 26]. The microstructural analysis of all the samples was done by using the conventional field emission scanning electron microscopy (FESEM, Nova. SEM450, FEI, USA), transmission electron microscopy (TEM, JEM-2100, JEOL, Japan, 300 kV), and high-resolution transmission electron microscopy (HRTEM) techniques. A conventional FTIR spectrometer (JASCO FT IR 460 + Spectrophotometer, Easton, MD, USA; resolution 4 cm^{-1} , range $500\text{--}4000 \text{ cm}^{-1}$) was used to identify the presence of the various chemical bonds and functional groups present in the surfaces of the samples. The studies on thermally induced phase changes and associated dissociation processes were conducted by the differential thermal analysis (DTA), and thermo-gravimetric analysis (TGA) of the samples using a conventional simultaneous thermal analyzer (Shimadzu DTH 60H, Japan; room temperature to 800°C

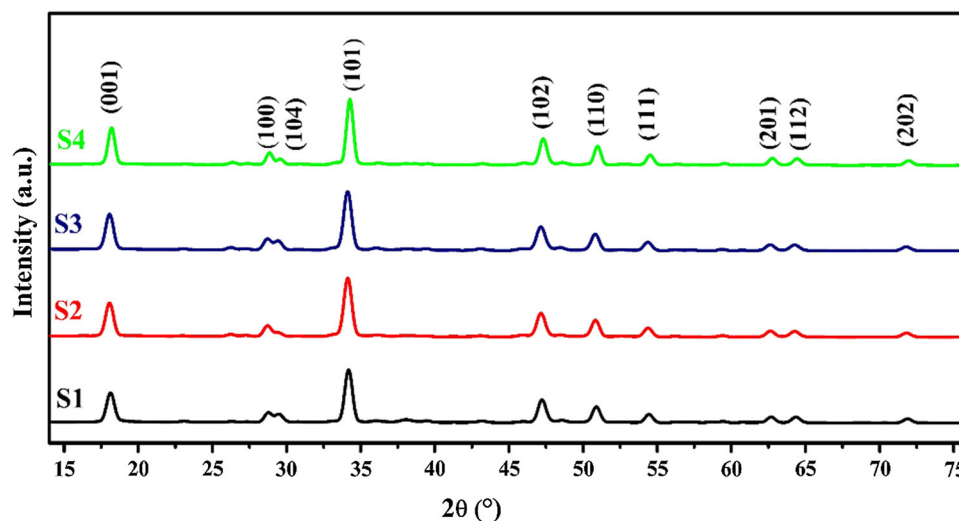
in the air; heating rate— $10^\circ\text{C}/\text{min}$, cooling rate— $10^\circ\text{C}/\text{min}$) was used. The optical characterizations of the samples were done by the well-known ultraviolet–visible (UV–Vis) spectroscopy (Shimadzu, UV-NIR 2600, Japan; wavelength range of $190\text{--}800 \text{ nm}$) technique by using the Tauc plots for direct band gap (Eg). The antimicrobial efficacies of the samples S1, S2, S3, and S4 were studied against a Gram-negative bacteria, e.g., *Escherichia coli* (*E. coli*, Microbial type culture collection, CSIR-IMTECH, Chandigarh, India) by the conventional agar plate well diffusion method with Ca(OH)_2 concentrations of CN0, CN1, CN2, and CN3 (e.g., 1, 10, 50 and 100 mg.ml^{-1} , respectively). However, out of these concentrations as the results presented later will show that at the concentration of CN0, there was no appreciable efficacy at any of the experimental conditions studied in the present work. Therefore, experimental data were collected for the other remaining three concentrations of, e.g., CN1, CN2, and CN3. After 6 h, the diameter of the first zone of inhibition was measured with a ruler. Thus, the diameters (D_{iz}) of the zones of inhibitions were measured as a function of various equal and unequal exposure periods, e.g., 6, 18, 22, 42, and 48 h [13, 24]. All antimicrobial efficacy testing experiments were repeated three times, and the average data were taken. Wherever relevant, the scatters in these data are represented in the relevant plots as ± 1 standard deviation.

Results and discussion

XRD analysis

The XRD spectra of samples S1, S2, S3, and S4 are shown in Fig. 1. The peaks in Fig. 1 exhibit the hexagonal Ca(OH)_2 as the major phase (Space group p-3 m1, Space Group No: 164, PDF Card No. 00-004-0733) and the rhombohedral calcite (CaCO_3) phase (Space group R-3C, Space Group No: 167, PDF Card No. 00-005-0586) as the minor phase in all the samples [23, 24]. The data on the analysis of the XRD for various planes of the different Ca(OH)_2 powders by the conventional Scherrer's method are shown in Table 1. Here, (t) represents the crystallite size and (d) represents the interplanar spacing. Averaged across the planes, the crystallite sizes (t) are about 32.8, 29.7, 29.9, and 31 nm in the samples S1, S2, S3,

Figure 1 XRD patterns of the samples S1, S2, S3, and S4.



and S4, respectively. Similarly, the average interplanar spacings (d) are about 0.212, 0.211, 0.212, and 0.211 nm, respectively. The (d) values are not significantly sensitive to the variation in molarity of the samples S1, S2, S3, and S4 because all of them represent phase pure $\text{Ca}(\text{OH})_2$ powders only (Fig. 1). The dislocation density (ρ) of samples S1, S2, S3, and S4 is evaluated as $\sim 0.7539 \times 10^{15}$, 0.5862×10^{15} , 0.4423×10^{15} , and 0.3717×10^{15} lines m^{-2} , respectively. Thus, the dislocation density data corroborate well with the crystallite size data obtained from the XRD spectra [25]. The smaller crystallite size provides accommodation of more dislocations per unit area. Therefore, it is expected that dislocation density decreases with a simultaneous increase in molarities of both precursor and precipitator solutions. According to the W-H plots (Fig. 2a, b, c, and d), the crystallite sizes are about 36, 41, 48, and 52 nm for the samples S1, S2, S3, and S4, respectively [26]. The W-H analysis data and dislocation density of all samples are given in Table 2. From the data plotted in Figs. 1, and 2 and presented in Tables 1 and 2, it is concluded that synthesized powders are generally nanocrystalline in nature and the crystallite sizes enhance with a simultaneous increase in the molarity of both precursor and precipitator solutions [25]. However, akin to the dislocation density, the dimensionless lattice strain values estimated as, e.g., 6.4×10^{-4} , 5.875×10^{-4} , 5.725×10^{-4} , and 5.45×10^{-4} [25, 26], in turn for the samples S1, S2, S3, and S4 (Fig. 3) reduce with a simultaneous increase in the molarity of both precursor and precipitator solutions, as expected. The probability of having more reactions per unit time

increases with an increase in equimolar concentrations of the reactants. As a result, the possibility of having more calcium hydroxide formation per unit of time increases with an increase in the equimolar concentration of the reactants. Thus, to accommodate this physical process the crystallite size of calcium hydroxide increases with an increase in the equimolar concentration of the reactants (Fig. 3). Since dislocation density is inversely proportional to crystallite size, it follows that dislocation density should decrease with an increase in molar concentration of the reactants (Fig. 3). Also, an increase in crystallite size implies a smaller surface-to-volume ratio. The smaller is the surface-to-volume ratio the lesser is the presence of dislocation network in the crystallites. Further, the lattice strain is inversely proportional to crystallite size [24–26]. Hence, it is expected that lattice strain decreases with an increase in equimolar concentrations of the reactants, as is also confirmed from the experimental data (Fig. 3). It is also a fact that the lesser is the presence of a dislocation network, the more relaxed is the local microstructure. The more relaxed the local microstructure is, the smaller is the average strain. However, the nature of lattice strain remains all through positive, i.e., tensile (Fig. 3) as the crystallite size increases monotonically. This physical process also suggests that the comparatively larger crystallites continuously try to accommodate themselves within the fixed lattice volume of calcium hydroxide. So, the lattice strain remains tensile with the increase in the equimolar concentration of the reactants.

Table 1 XRD data analysis of the various $\text{Ca}(\text{OH})_2$ powders by Scherrer's method

Sample	(001)		(100)		(104)		(101)		(102)		(110)		(111)		(201)		(112)		(202)	
	<i>t</i>	<i>d</i>	<i>T</i>	<i>d</i>	<i>t</i>	<i>d</i>	<i>t</i>	<i>d</i>	<i>t</i>	<i>d</i>	<i>t</i>	<i>d</i>	<i>t</i>	<i>d</i>	<i>t</i>	<i>d</i>	<i>t</i>	<i>d</i>	<i>t</i>	<i>d</i>
S1	34.0386	4.8388	38.3188	3.2094	26.1157	1.0698	36.9356	2.6204	31.1758	1.8529	34.6922	1.8529	34.6899	1.7155	33.1518	1.5129	28.1473	1.4352	31.3264	1.3102
S2	32.9536	4.8454	38.0919	3.2144	28.2644	1.0713	31.6658	2.6244	24.6858	1.8557	32.4131	1.8558	29.7930	1.7181	28.4432	1.5152	23.1485	1.4374	26.9967	1.3122
S3	32.7435	4.8464	36.9804	3.2151	27.5389	1.0716	30.6464	2.6250	22.5088	1.8561	31.0272	1.8562	28.6915	1.7185	27.9473	1.5156	22.2041	1.4377	27.7163	1.3125
S4	31.9531	4.8282	40.9752	3.2016	32.6376	1.0673	33.4358	2.6141	25.5161	1.8485	34.5929	1.8484	30.1566	1.7113	29.7761	1.5092	23.4267	1.4318	27.2048	1.3070

t crystallite size by Scherrer's method (nm), *d* interplanar spacing (Å)

Microstructural studies

FESEM study

The FESEM photomicrographs shown in Fig. 4a, b, c, and d depict, respectively, the typical granular microstructures of the samples S1, S2, S3, and S4. The grain size of all the samples is determined using ImageJ software to study the size distribution, and the histogram of the same between particle size and counts of particle is shown in the inset of Fig. 4. The minimum feature size is lesser than or equal to about 40 nm (e.g., Fig. 4a), while the maximum feature size is greater than or equal to about 500 nm (e.g., Fig. 4d). The smaller the crystallite size the smaller is the feature size due to the presence of large tensile lattice strain (Fig. 4a) and vice versa (Fig. 4b, c, and d). There is a surface charge on the nanocrystalline powders (Figs. 3, and 4). So, the agglomeration occurs due to the Van der Waals interaction at the level of local microstructure. Hence, the granules most likely form from localized agglomerates of nanocrystalline powders. The granule size enhances with an increase in molarity (Fig. 4b). Further, these clusters tend to pose in a layered structure as is expected for the hexagonal $\text{Ca}(\text{OH})_2$ phase (Fig. 4c). Furthermore, the decrease in localized strain helps the proximity of the individual layers to be possible (Figs. 3 and 4c). The crystallite size (Fig. 3) and the granule size (Fig. 4d) are the highest in sample S4 which exhibits large numbers of hexagonal structure formations in multiple layers that are very close to each other as they experience the least amount of local tensile strain. Thus, the observations made from the FESEM photomicrographs (Fig. 4) corroborate well with the XRD data (Figs. 1, 2, and 3).

TEM study

As a typical illustrative example, the TEM and HRTEM photomicrographs obtained for the samples S1 and S3 are shown in Fig. 5a, b, c, d, e, and f, respectively. As expected, the structure is hexagonal (Fig. 5a, d) with a feature size of $\sim 40 \leq S \leq 500$ nm, akin to the FESEM observations (Fig. 4a, c). Undoubtedly, the major phase is hexagonal $\text{Ca}(\text{OH})_2$ as confirmed by the corresponding polycrystalline SAED pattern of S1 (Fig. 5b) which corroborates well with the XRD data (Fig. 1). The presence of (101) and (202) planes with respective *d* values of ~ 0.278

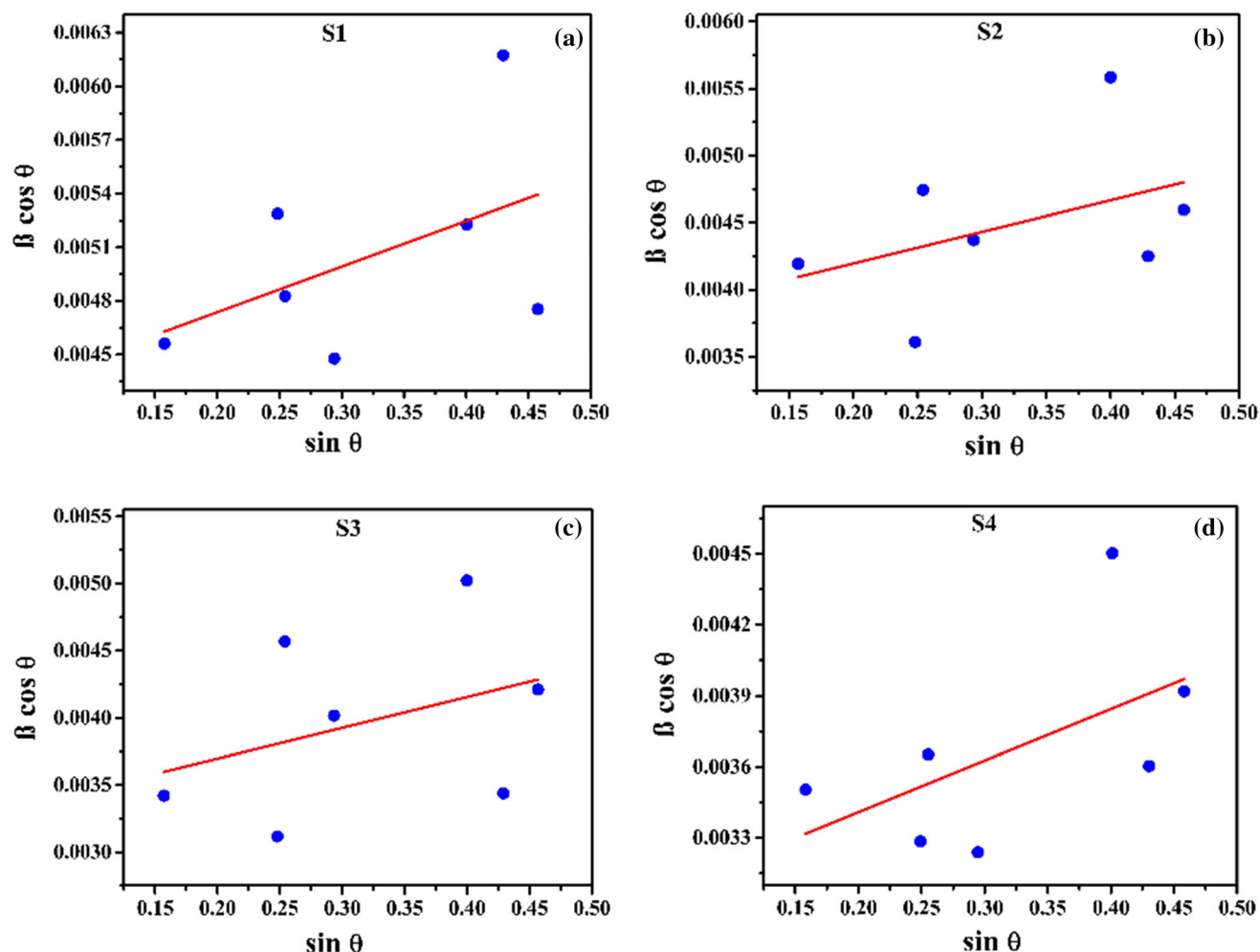


Figure 2 Williamson–Hall plots of the samples S1, S2, S3, and S4.

Table 2 Analysis of XRD data of the various Ca(OH)_2 powders by W-H plots

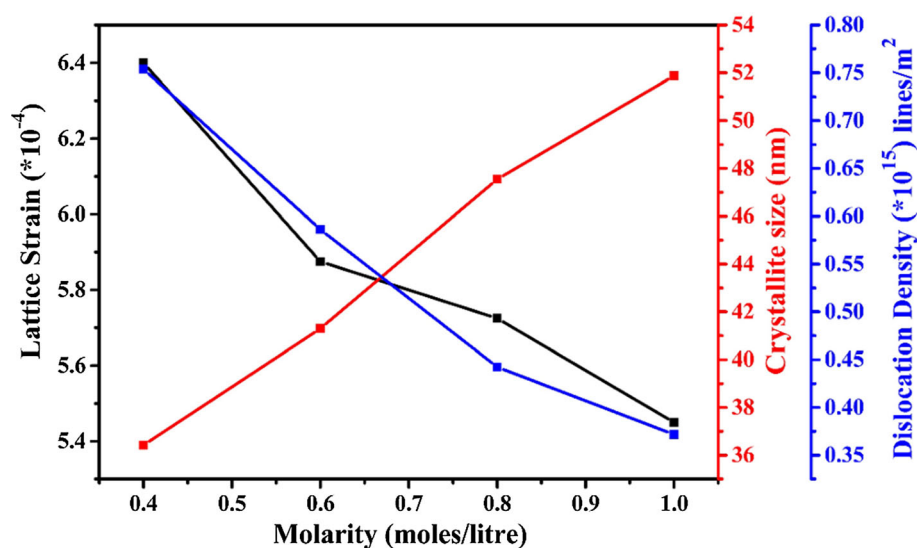
Sample	Molarity	Lattice strain ($\times 10^{-4}$)	a (nm)	C (nm)	Crystallite size by W-H plot (nm)	Dislocation density ($\times 10^{15}$ lines/ m^2)
S1	0.4	6.4	0.37059	0.48388	36.4208	0.75388
S2	0.6	5.875	0.37117	0.48454	41.30295	0.58619
S3	0.8	5.725	0.37125	0.48464	47.54938	0.44229
S4	1.0	5.45	0.36969	0.48282	51.87205	0.37165

and ~ 0.130 nm is evident in the SAED pattern (Fig. 5b). The HRTEM fringe patterns (Fig. 5c) exhibit (101) and (100) planes with respective (d) values of ~ 0.254 nm and ~ 0.311 nm which are those of ~ 0.262 nm and 0.320 nm obtained from the XRD data (Fig. 1) in correspondence. Similar statements are true for the SAED pattern (Fig. 5e) and HRTEM fringe pattern (Fig. 5f) of the sample S3.

FTIR study

The FTIR spectra for the samples S1, S2, S3, and S4 are shown in Fig. 6a, b, c, and d. The characteristic bands at ~ 3630 cm^{-1} correspond to the sharp OH group stretching mode [16, 17]. The minor absorption bands at around 2330 cm^{-1} occur due to stretching vibrations of atmospheric CO_2 adsorption on the powders [18] while the minor absorption bands

Figure 3 The variations of lattice strain, crystallite size, and dislocation density as a function of molarity of the precursor and precipitator solutions.



at $\sim 1694 \text{ cm}^{-1}$ occur due to $\text{C}=\text{O}$ stretching vibrations in the samples S1, S2, S3, and S4 [19]. Further, the absorption bands at ~ 1450 to 1520 cm^{-1} occur due to the characteristic ν_3 asymmetric stretching of the surface adsorbed CO_3 group [16–19] while the bands at ~ 850 to 875 cm^{-1} occur due to the characteristic ν_2 symmetric deformation of the surface adsorbed CO_3 group [16–19]. The absorption bands present at about 460 cm^{-1} occur due to the stretching vibration of the $\text{Ca}-\text{O}$ bond [16]. The recent observations match well with literature reports [16–20]. The FTIR spectra of all the samples show the characteristics of both hydroxide and carbonate groups of calcium, as expected.

Thermal behavior

The DTA-TGA plots for the samples S1, S2, S3, and S4 are shown, respectively, in Fig. 7a, b, c, and d. A comparison of the results plotted in Fig. 7a, b, c, and d shows that the initiation temperature for structural water loss decreases from, e.g., $\sim 420^\circ\text{C}$ in the sample S1 to 414°C in the sample S2 to 393°C in the sample S3 to 378°C in the sample S4. Similarly, the completion temperature for structural water loss decreases from, e.g., $\sim 481^\circ\text{C}$ in the sample S1 to 456°C in the sample S2 to 456°C in the sample S3 to 451°C in the sample S4.

This decrease occurs in tandem with the decrease in the corresponding DTA-based phase transformation initiation temperature of hexagonal $\text{Ca}(\text{OH})_2$ to cubic CaO phases, e.g., $\sim 415^\circ\text{C}$ in the sample S1 to 411°C in the sample S2 to 379°C in the sample S3 to

377°C in the sample S4. Further, this decrease is also in tandem with the decrease in the corresponding DTA-based phase transformation completion temperature of hexagonal $\text{Ca}(\text{OH})_2$ to cubic CaO phases, e.g., $\sim 460^\circ\text{C}$ in the sample S1 to 457°C in the sample S2 to 442°C in the sample S3 to 439°C in the sample S4. Here it is worth recalling that the nanocrystallite sizes are, e.g., $\sim 36, 41, 48$, and 52 nm for the samples S1, S2, S3, and S4. Thus, according to both the TGA and the DTA data (Fig. 7a, b, c, and d), the phase transformation temperature decreases with the increase in the nanocrystallite size. Further, it is seen from the data plotted in Fig. 8 that the relative degree of crystallinity drops from about 100% in the sample S1 to 86% in the sample S2 to 83% in the sample S3 to about 80% in the sample S4 (Fig. 1, [24]) as the nanocrystallite size increases. In a similar fashion, as mentioned earlier, the DTA-based phase transition initiation temperature decreases with an increase in nanocrystallite size of the various $\text{Ca}(\text{OH})_2$ powders. Therefore, the higher the relative degree of crystallinity in a given $\text{Ca}(\text{OH})_2$ sample, the higher the phase transformation initiation temperature and vice versa. The relatively higher degree of crystallinity of sample S1 is reflected in the absence of microstructural defects in FESEM (Fig. 8 inset, a) and TEM (Fig. 8 inset, c) photomicrographs, while the relatively lower degree of crystallinity of sample S3 is reflected in the presence of microstructural defects in FESEM (Fig. 8 inset, b) and TEM (Fig. 8 inset, d) photomicrographs. Indeed, other researchers [24] also note that the $\text{Ca}(\text{OH})_2$ sample with a relatively

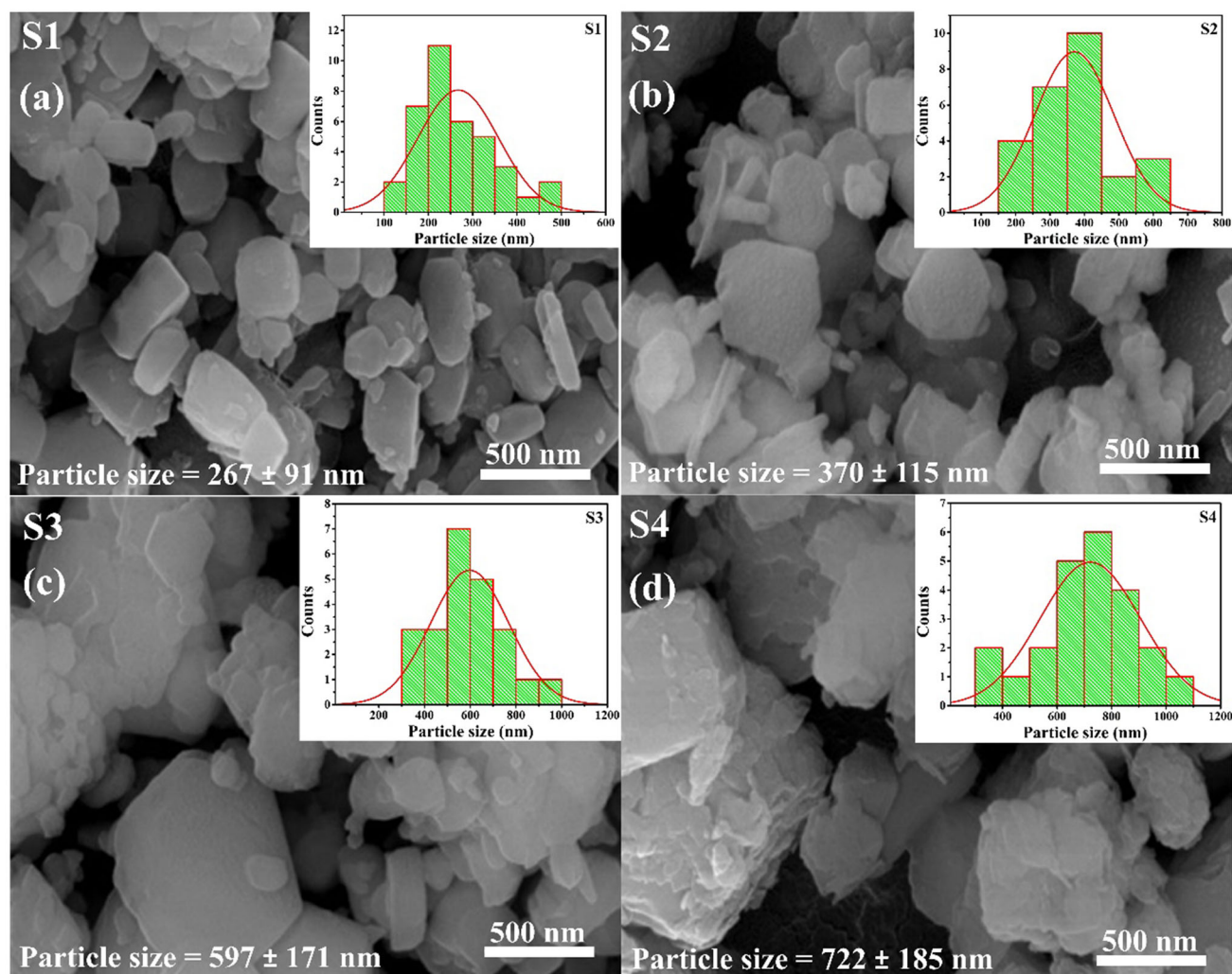


Figure 4 FESEM photomicrographs of samples S1, S2, S3, and S4.

higher degree of crystallinity shows the phase transformation start, peak, and end temperatures of, e.g., 299, 454, and 501 °C, respectively. This proposition holds good not only for $\text{Ca}(\text{OH})_2$ [24] but also for CaCO_3 [25] as well as a truly wide variety of clay and other minerals [26].

Optical behavior

From the UV–Vis spectra (Supplementary Fig. S1a, b, c, and d) and the corresponding Tauc plots (Supplementary Fig. S2a, b, c, and d), the direct optical band gap energy (E_g) values of the samples S1, S2, S3, and S4 are evaluated as ~ 5.74 , 5.90, 5.73, and 5.25 eV in turn. Therefore, the optical band gap generally decreases with an increase in molarity because the nanocrystallite size increases (Fig. 9), as expected.

These data (Fig. 9) are comparable to ~ 5.81 eV reported [20] for $\text{Ca}(\text{OH})_2$ nanopowders. It also compares well with theoretical predictions of 7.3 to 7.6 eV [27]. As the particle size decreases the gap between the valence and conduction bands increases. Therefore, the band gap energy value increases (Fig. 9). Similar prediction is made also by a host of very detailed theoretical considerations [28–30]. It is worth recalling here that the degree of crystallinity decreases, i.e., defect increases as the nanocrystallite size increases (Figs. 8, and 9). Thus, the current data also confirm that the presence of defects decreases the bandgap in various nanomaterials [31–34]. These results are also consistent with structural (Figs. 1, 2, and 3), microstructural (Figs. 4 and 5), surface functional (Fig. 6), thermal (Figs. 7 and 8), and optical

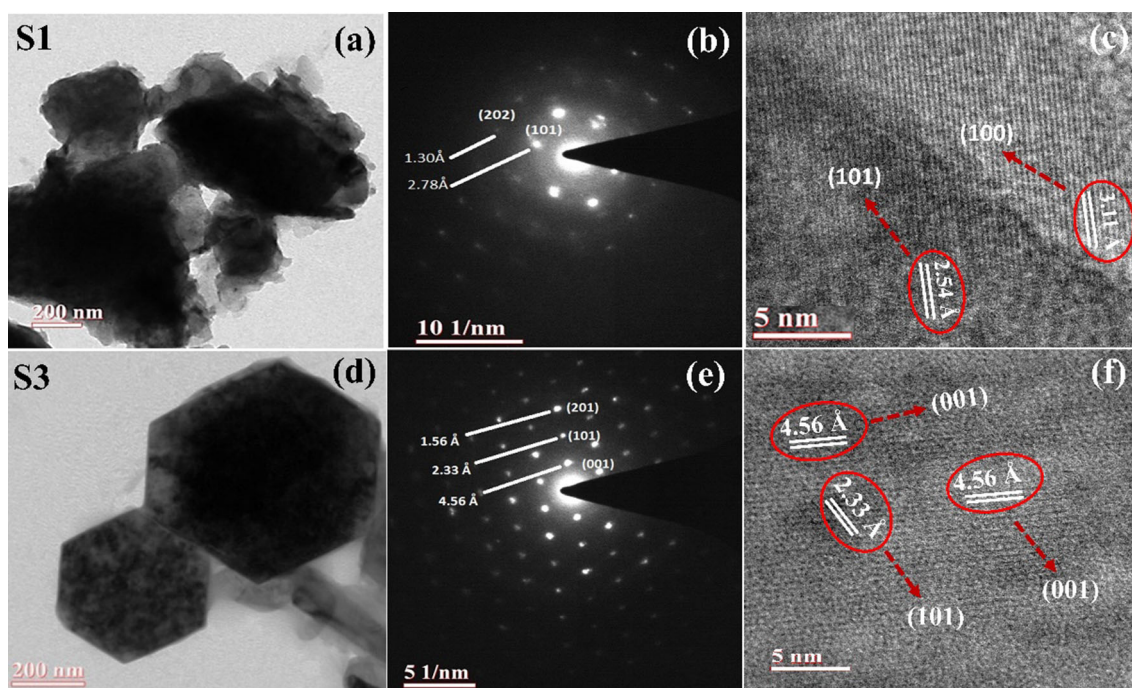


Figure 5 Microstructural analysis of the synthesized Ca(OH)_2 : for sample S1 **a** bright-field TEM micrograph, **b** SAED pattern, **c** HRTEM image; and for sample S3 **d** bright-field TEM micrograph, **e** SAED pattern, **f** HRTEM image.

(Fig. 9) characteristics of the present nano- Ca(OH)_2 powders, as discussed above.

Antimicrobial activity of nano-calcium hydroxide materials

The inhibition zone diameters (D_{iz}) of the samples S1, S2, S3, and S4 as a function of concentration (e.g., CN1, CN2, and CN3) are shown, respectively, in Supplementary Fig. S3a, b, c, and d with parametric variations in exposure times, i.e., 6, 18, 22, 42, and 48 h. The corresponding insets show the corresponding optical photomicrographs. These optical photomicrographs are all taken at the same magnification as indicated by the corresponding scale pictures given in the insets. The samples exhibit different antimicrobial behavior in terms of (D_{iz}), (Supplementary Fig. S3a, b, c, and d). This behavior is expected from the differences in nanocrystallite sizes (Fig. 3), differences in microstructures (Figs. 4, and 5), relative differences in the presence of surface-OH groups (Fig. 6), differences in the degree of crystallinity (Fig. 8), defect structure (Fig. 8), and band gap energy values (Supplementary Figs. S1, S2 and Fig. 9). This expectation is also consistent with the

antimicrobial behavior of different nano-oxides and hydroxides reported by various researchers [35–38].

In the case of sample S1, the maximum bacterial growth inhibition occurs after 6 h (Supplementary Fig. S3a). But this bactericidal activity reduces by $\sim 7\%$ after 18 h followed by a further decrease of $\sim 6.5\%$ up to 22 h of exposure. However, the variations in (D_{iz}) remain bacteriostatic thereafter up to 48 h of exposure. The variations in (D_{iz}) become bacteriostatic after 18 h of exposure for all the three concentrations (Supplementary Fig. S3a). The minimum magnitude of (D_{iz}) $\sim 5.5 \pm 0.21$ mm occurs after 22-h exposure for the concentration CN1 while the maximum magnitude of (D_{iz}) $\sim 11.5 \pm 0.70$ mm occurs after 6-h exposure for the concentration CN3 (Supplementary Fig. S3a).

In the case of the sample S2 after 6 h, there occurs an abrupt increase of 18% in the bactericidal activity at 18 h at the concentration CN1 (Supplementary Fig. S3b). This activity remains stable till 22 h of exposure. Thereafter, it decreases by 45% after 42 h of exposure. The minimum magnitude of (D_{iz}) $\sim 3 \pm 0.42$ mm in CN1 occurs after 42-h exposure, and its magnitude does not change even after an exposure period of 48 h (Supplementary Fig. S3b). At concentrations of CN2 and CN3, profound analogous

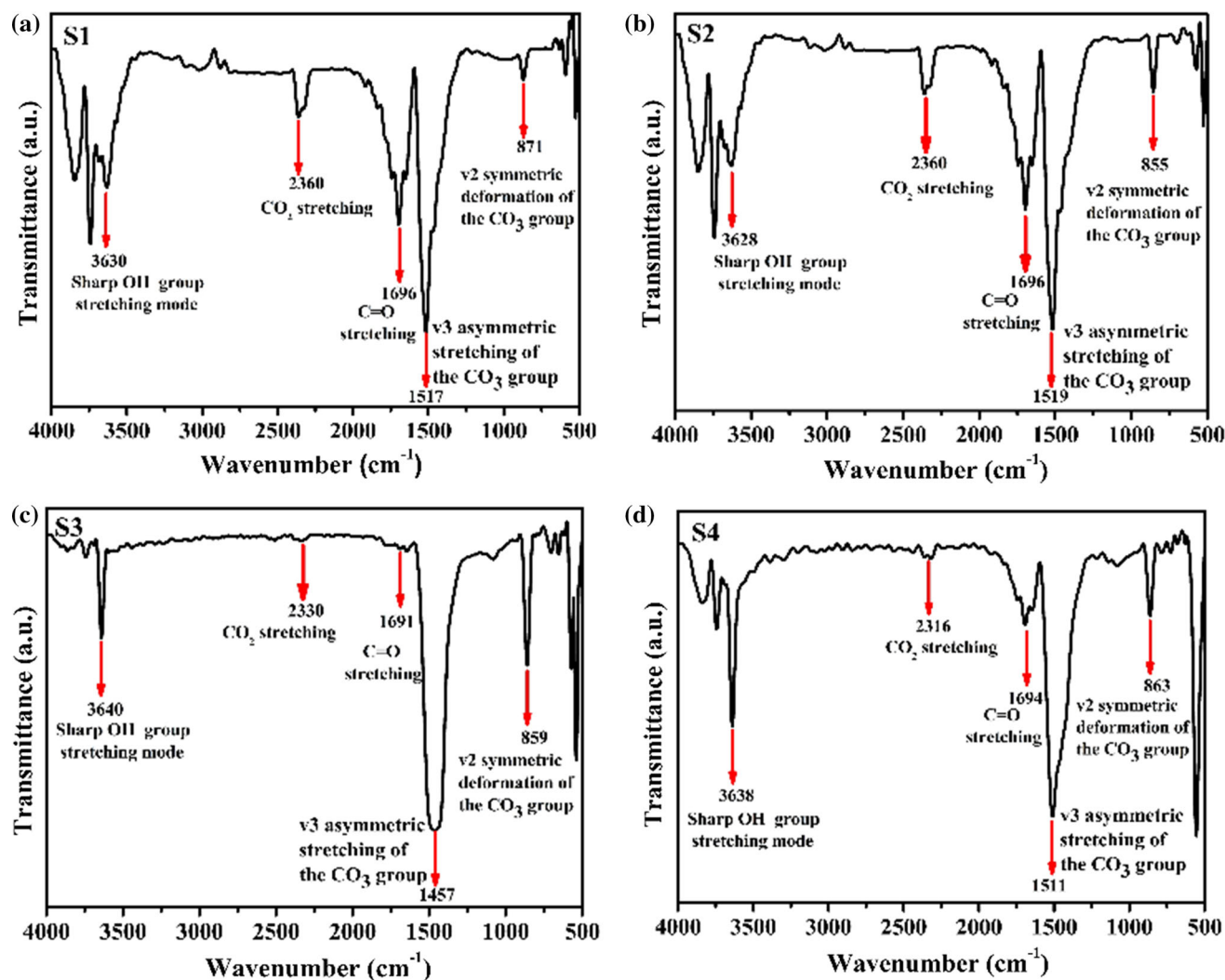


Figure 6 The FTIR spectra of the samples S1, S2, S3, and S4.

antimicrobial activities are noted although relative numerical magnitudes are different in correspondence. This activity enhances with the increase in concentration from CN2 to CN3. On the other hand, the maximum magnitude of (D_{iz}) $\sim 12 \pm 0.42$ mm occurs right after 6-h exposure for the concentration CN3 and it does not change even after an exposure period of 48 h (Supplementary Fig. S3b).

In the case of sample S3, there is bactericidal activity after 6 h of exposure at concentration CN1 (Supplementary Fig. S3c). In addition, (D_{iz}) increases further by 8.3% due to the bactericidal activity after 18 h of exposure and the behavior remains bacteriostatic thereafter up to 48 h of exposure time. The pattern remains similar for the concentration of CN2 and CN3, although the relative magnitudes of (D_{iz}) are obviously different (Supplementary Fig. S3c). The

minimum magnitude of (D_{iz}) $\sim 5.5 \pm 0.70$ mm occurs after 6 h of exposure at concentration CN1. On the other hand, the maximum magnitude of (D_{iz}) $\sim 15 \pm 0.28$ mm occurs right after 18 h of exposure at concentration CN3 and it does not change even after an exposure period of 48 h (Supplementary Fig. S3c).

In the case of sample S4, bacterial growth inhibition occurs after 6 h of treatment at concentration CN1 (Supplementary Fig. S3d) and the magnitude of (D_{iz}) does not change further for exposure up to 18 h. Thereafter, due to enhanced bactericidal activity (D_{iz}) increases by 11% at 22 h of exposure followed by a bacteriostatic behavior up to 48 h of further exposure. For a constant exposure period of 6 h, the bactericidal activity becomes comparatively pronounced at concentration CN2 by 60% and by 66% at concentration

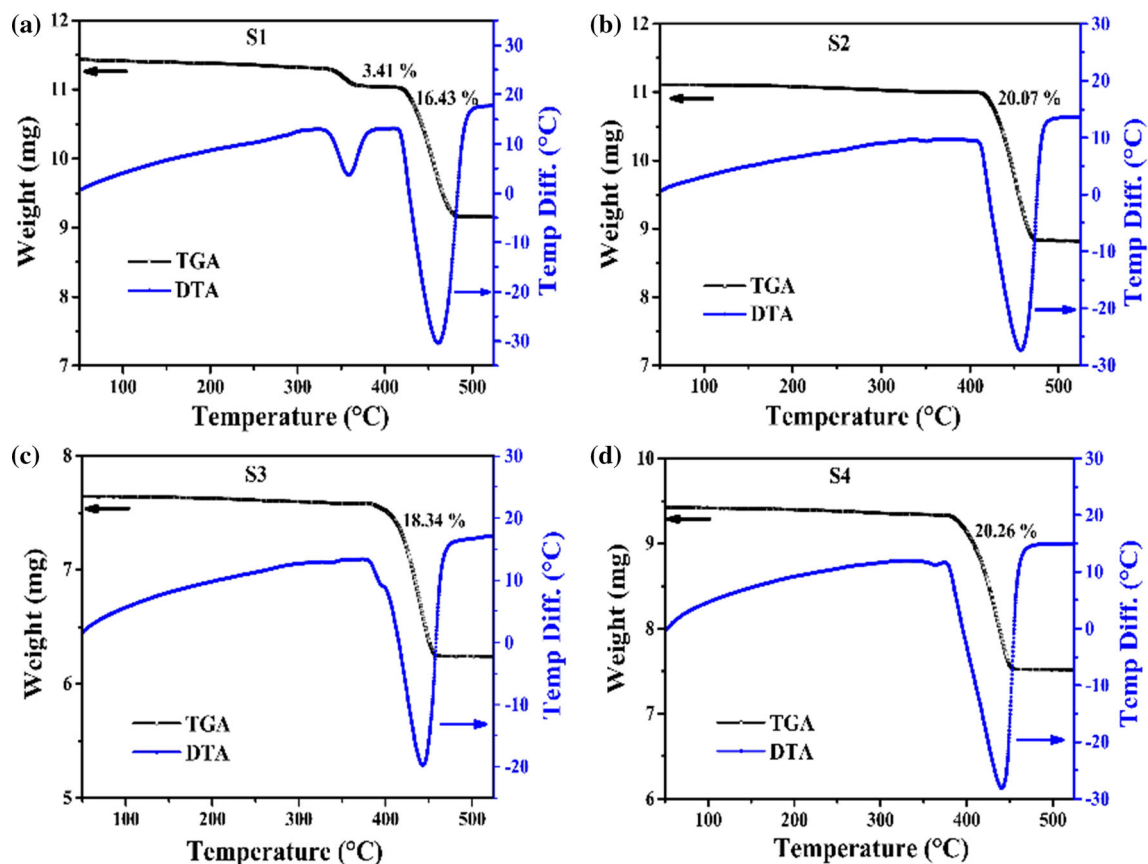


Figure 7 TGA-DTA plots of the samples S1, S2, S3, and S4.

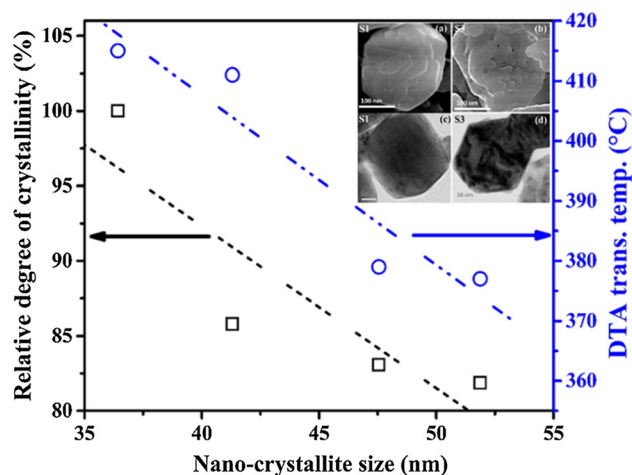


Figure 8 Relative degree of crystallinity and DTA transition temperature variation with respect to nanocrystallite sizes of the samples S1, S2, S3, and S4 samples. Inset: FESEM photomicrograph of sample a S1, b S3 and HRTEM images of samples c S1 and, d S3.

C3 in comparison with the 6-h exposure at CN1 concentration (Supplementary Fig. S3a, b, c, and d).

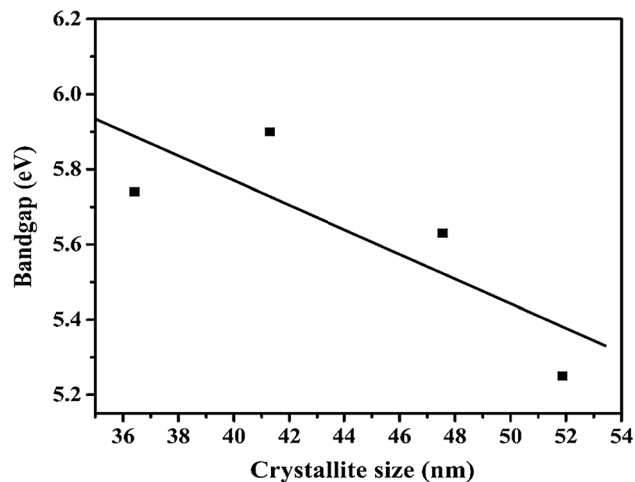


Figure 9 Optical band gap energy (E_g) variation with respect to the nanocrystallite size of $\text{Ca}(\text{OH})_2$.

Further, the variations in (D_{iz}) become bacteriostatic after 42 h of exposure at concentrations of CN2 and CN3, although their magnitudes are obviously different (Supplementary Fig. S3a, b, c, and d). Thus, the

different samples have relatively different antimicrobial behavior.

The different antimicrobial behaviors of the different samples may be rationalized in terms of the variations in two factors. The first is the differences in their relative abilities to generate reactive oxygen species (ROS) [20, 35–38]. The second one is the variations in their relative exposures of crystal edges to *E. coli*. This is obviously dependent in a complex fashion on several other factors. These factors include, for instance, the variations in the electronic band structure and hence, the band gap energy values, the microstructures, the nanocrystallite sizes, the propensity of localized defects in the microstructure, and the ease of availability of hydroxyl ions at the surface of the different samples (Figs. 1, 2, 3, 4, 5, 6, 7, 8, and 9 [35–38]). Furthermore, the hexagonal structure has an advantage over other types of surfaces. Since the hexagonal structure has sharp edges and more charges tend to accumulate on these sharp

edges that help in enhancing the interaction with the microbe surface that resulting in better antimicrobial activities of the materials. Similar observations have been reported [39–41] by several authors for hexagonal structure. These aspects shall be discussed in further detail later in the present work.

Influence of variations in nanocrystallite size on antimicrobial efficacy

For a change in concentration from CN1 to CN2 for an exposure period of 6 h, the (%) increase in (D_{iz}) increases from about 62% in S1 to 120% in S2 to 100% in S3 to 150% in S4 (Fig. 10a, b, c, and d). Thus, the (%) increase in (D_{iz}) increases generally with the increase in nanocrystallite size (Fig. 10a, b, c, and d). For the same change in concentration after 18 h of exposure, the (%) increase in (D_{iz}) increases from about 58% in S1 to 80% in S2 to 100% in S3 to 110% in S4. Under the same condition of concentration change for 22 h of exposure, the (%) increase in (D_{iz}) increases from about 64% in S1 to

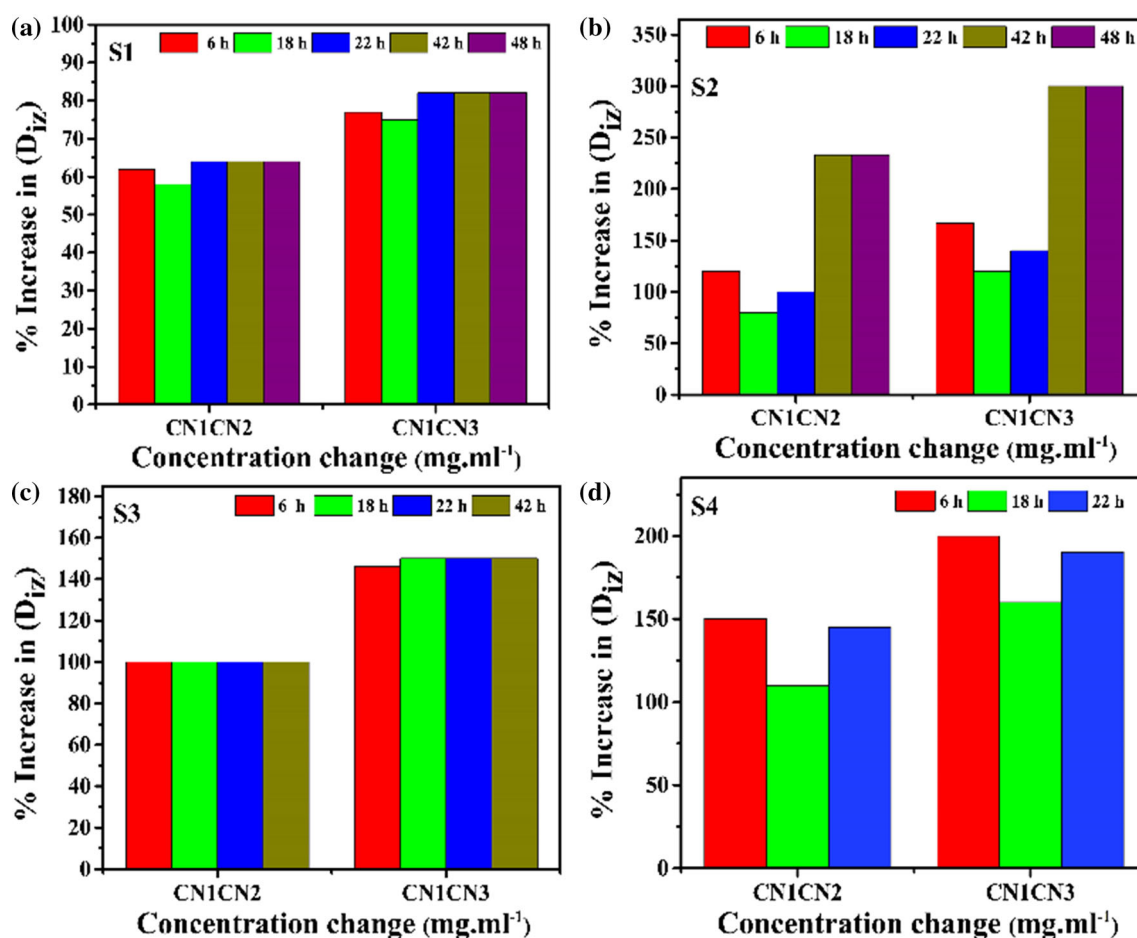


Figure 10 Increase in inhibition zone diameter with respect to concentration changes for the samples S1, S2, S3, and S4.

100% in S2 to 100% in S3 to 145% in S4 (Fig. 10a, b, c, and d). Further, under the same condition of concentration change for 42 h of exposure the (%) increase in (D_{iz}) increases from about 64% in S1 to 233% in S2 to 100% in S3. Therefore, the trend of data remains similar to those obtained after 6 h of exposure concerning the increase in nanocrystallite sizes. Similar observations are also reported by other researchers in the case of nano-Mg(OH)₂ [37]. For a change in concentration from CN1 to CN3 for an exposure period of 6 h, the (%) increase in (D_{iz}) increases from about 77% in S1 to 167% in S2 to 146% in S3 to 200% in S4 (Fig. 10a, b, c, and d). For the same change in concentration after 18 h of exposure, the (%) increase in (D_{iz}) increases from about 75% in S1 to 120% in S2 to 150% in S3 to 160% in S4. Further, for the same change in concentration after 22 h of exposure, the (%) increase in (D_{iz}) increases from about 82% in S1 to 140% in S2 to 150% in S3 to 190% in S4 (Fig. 10a, b, c, and d). Furthermore, for the same change in concentration after 42 h of exposure, the (%) increase in (D_{iz}) increases from about 82% in S1 to 300% in S2 to 150% in S3. Thus, here also the (%) increase in (D_{iz}) enhances generally with the increase in nanocrystallite sizes as also reported by other researchers in the case of nano-Mg(OH)₂ [37]. To compare the effect of antimicrobial efficacy of nano-size particles and micro/larger particles, a sample using 3 M concentration of the Ca(NO₃)₂·4H₂O solution and NaOH solution was synthesized. This is termed as 3 M sample in subsequent discussions. All of the samples (0.4 M, 0.6 M, 0.8 M, 1.0 M, and 3.0 M) were tested at the same concentration of 100 mg/ml. Supplementary Fig. S4 depicts the inhibition zone diameter of all samples as a function of time, while Supplementary Fig. S5a, b depicts the inhibition zone diameter (D_{iz}) and % change in (D_{iz}) with respect to molarity change, respectively. The diameter of the inhibition zone illustrates that antibacterial efficiency improves up to a point with increasing molarity. However, in case of further increase in molarity, i.e., 3 M sample which has a larger crystallite size, the antibacterial efficiency decreases which can be clearly seen from Supplementary Figs. S4 and S5. Supplementary Fig. S6a depicts the XRD pattern of 3 M calcium hydroxide sample, whereas Supplementary Fig. S6b depicts the W-H plot of the same sample. The crystallite size and lattice strain of the synthesized 3 M sample calculated from the W-H plot were found to be 75 nm and

0.00149, respectively. The FESEM picture and size distribution curve of the sample is also shown in Supplementary Fig. S6c. This FESEM photomicrograph confirms the bigger crystallite size of the sample as the molarity is raised.

Influence of Variations in Exposure Time on Antimicrobial Efficacy

It is interesting to note that out of the four samples three samples show a general trend of the initial increase in (D_{iz}) values, i.e., an enhancement in antimicrobial efficacy with an increase in exposure time prior to stabilization (Supplementary Figs. S3a, b, c, d and Fig. 10a, b, c, and d). These results may be rationalized based on the fact that more exposure time provides higher contact times for the nano-Ca(OH)₂ powder samples with the *E. coli*. The saturation occurs possibly because all the available interaction sites are consumed up, thereby leading to a bacteriostatic situation. However, sample S1 shows slightly different behavior in comparison with those of S2, S3, and S4 reported above. It also possesses the smallest nanocrystallite size (Fig. 3), the highest degree of crystallinity (Fig. 8), and the highest magnitude of optical band gap energy (Fig. 9). In this case for all the concentrations, the magnitude of (D_{iz}) is highest after 6 h of exposure and then it reduces slightly after 18 h of exposure prior to having saturation at a slightly more reduced magnitude at higher exposure periods of, e.g., 22, 42, and 48 h (Supplementary Fig. S3a, b, c, and d). Thus, the antimicrobial efficacy of S1 reduces very slightly by about (e.g., 8%, 5%, and 4% for CN1, CN2, and CN3 in turn) with an increase in exposure time up to 18 h prior to achieving bacteriostatic nature at exposure periods of 22 h and above. It also possesses the smallest nanocrystallite size. Other researchers also report the lowest antimicrobial efficacy for the nano-Mg(OH)₂ powders with the smallest particle size [37].

Effect of change of concentration on antimicrobial efficacy

Generally, for a given sample (e.g., S1, S2, S3, and S4), and given exposure time (T), the (D_{iz}) value increases with an increase in concentration (e.g., CN3 > CN2 > CN1) (Supplementary Fig. S3a, b, c, and d and Fig. 10). This is taken in the current work as a representative factor for a relative measure of antimicrobial efficacy. For instance, in the case of sample S1 for an exposure period of 6 h the (D_{iz}) value increases by about 62 and 77% as the concentration increases from CN1 to CN2, and from CN1 to

CN3. Depending on sample type, e.g., S2, S3, and S4, and the exposure period, e.g., 18, 22, 42, and 48 h, the relative percentage efficacies of course vary, but the overall trend remains valid (Supplementary Fig. S3a, b, c, and d and Fig. 10). Particularly, the data plotted in Fig. 10 confirm beyond any doubt that generally for a given exposure time (T) indeed the (D_{iz}) value increases with an increase in concentration (e.g., $CN3 > CN2 > CN1$). This happens because as the concentration increases; more number of nano- $Ca(OH)_2$ particles per unit area becomes available for antimicrobial activity exhibited by a given sample for a given exposure time (T). However, the efficacies slightly drop when the concentration change from CN2 to CN3 is considered. For instance, in the case of sample S1 for an exposure period of 6 h the (D_{iz}) value increases by only about 9.52% as the concentration increases from CN2 to CN3 (Supplementary Fig. S3a, b, c, and d and Fig. 10). As the exposure time increases to 18 h, the (D_{iz}) value increases only merely by about 10.5%. However, for exposure periods of, e.g., 22, 42, and 48 h, the increases in the (D_{iz}) value remain bacteriostatic at about 11.11% as the concentrations increase from CN2 to CN3 (Supplementary Fig. S3a and Fig. 10). Similar statements hold for all the other three samples (e.g., S2, S3, and S4) although the relative magnitudes of efficacies vary.

Rate of change of antimicrobial efficacy with respect to variations in concentration with parametric variation in exposure times Based on the experimental data presented in Supplementary Fig. S3a, b, c, and d, the rate of change of antimicrobial efficacy with respect to variations in concentration with parametric variation in exposure times can be calculated as $[d(D_{iz})/dCN]_T$ where CN represents concentration and D_{iz} represents the inhibition zone diameters. Further, $X = 1, 2$, and 3 , i.e., CN1 is 10, CN2 is 50, and CN3 is 100 mg.ml^{-1} , respectively. Furthermore, the exposure times T are, e.g., 6, 18, 22, 42, and 48 h as mentioned earlier. The rate of change in antimicrobial efficacy as a function of concentration change is plotted in Fig. 11a, b, c, and d for the samples S1, S2, S3, and S4.

Thus, in the case of the sample S1 exposed for 6-h exposure the rate of change in antimicrobial efficacy is given by, e.g., $(100 \text{ } \mu\text{m/mg ml}^{-1})$ as the concentration increases from CN1 to CN2. The rate of change drops to, e.g., $(87.5 \text{ } \mu\text{m/mg ml}^{-1})$ for an

exposure period of 18 h under the same concentration enhancement and remains the same, i.e., $(87.5 \text{ } \mu\text{m/mg ml}^{-1})$ for the exposure periods of 22, 42, and 48 h; Fig. 11a. These data again suggest the prevalence of the bacteriostatic nature of the antimicrobial activities (Supplementary Fig. S3a). For increase of concentration from CN2 to CN3, the rate of change in antimicrobial efficacy of the sample S1 drops to, e.g., $20 \text{ } \mu\text{m/mg ml}^{-1}$ and remains stationary there for the exposure periods of 6, 18, 22, 42, and 48 h. These data are plotted in Fig. 11a for sample S1. These data again suggest the prevalence of a bacteriostatic nature. Similar statements hold for all the other three samples (e.g., S2, S3, and S4) although the relative magnitudes of the rate of change in efficacies as a function of concentration change vary as depicted in turn in Fig. 11b, c, and d.

Mechanisms of antimicrobial activity

The major consensus from the literature [20, 35–63] is that the antimicrobial activity is triggered by reactive oxygen species (ROS) formation by most metal oxides and hydroxides. Based on these views only a qualitative, schematic picture of the antimicrobial activity mechanism is provided in Fig. 12a–n. Thus, a brief qualitative discussion only may follow. It is well known that atomic oxygen has two unpaired electrons. Now, these electrons stay in two different orbits. These orbits are in the outer electron shells of the atomic oxygen. In the perspective of nano- $Ca(OH)_2$ powders of the current work, the sequential reduction of oxygen through the addition of electrons can happen. These reductions provide the genesis of the various reactive oxygen species (ROS). If and when it happens, it can produce ROS like the superoxide ($O_2^{\cdot-}$), the singlet oxygen (1O_2), the hydrogen peroxide, the hydroxyl radical ($\cdot OH$) as well as the hydroxyl ion (OH^-), etc. [20, 53]. In the cases of Gram-positive, e.g., *Staphylococcus aureus* (*S. aureus*) and Gram-negative e.g., *Pseudomonas putida* (*P. putida*) bacteria it is opined [20] that both hydroxyl radical ($\cdot OH$) and singlet oxygen (1O_2) may provide major contributions to the antimicrobial activity of nano- $Ca(OH)_2$ powders while minor contribution may also come from the superoxide ($O_2^{\cdot-}$) species. In an aqueous solution, the hexagonal $Ca(OH)_2$ nanoparticles (Fig. 12a) dissociate into one Ca^{2+} ion and 2 ions of OH^- with a solution pH in the range of 12.5 to 12.8 (Fig. 12b), as mentioned above.

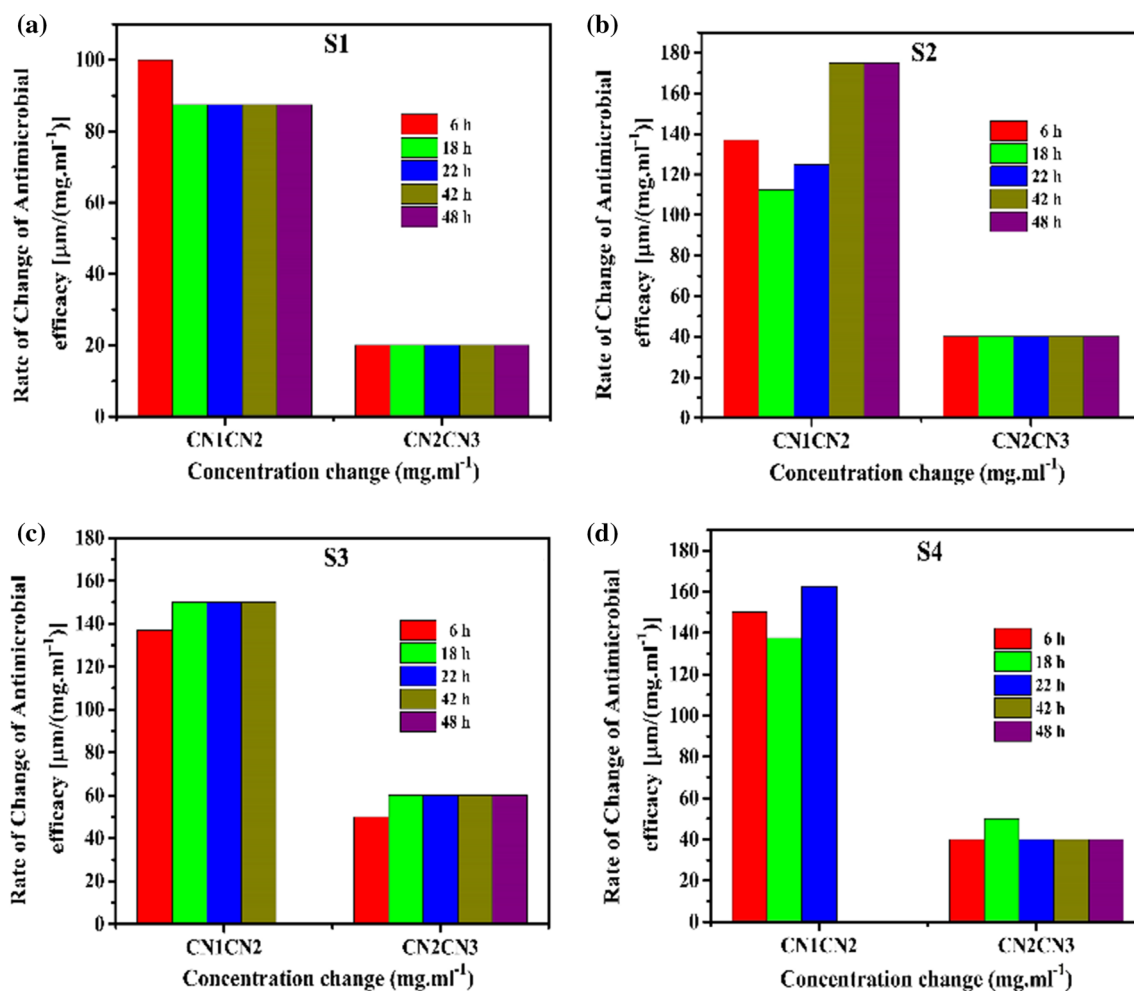


Figure 11 Rate of change of antimicrobial efficacy with respect to concentration changes for the samples S1, S2, S3, and S4.

The Ca^{2+} ions are positively charged. Hence, they can easily adhere to the negatively charged cell wall of *E. coli*. Simple calculations suggest that a reasonably large number of Ca^{2+} ions (e.g., 2.81×10^7) can assemble on the single *E. coli* cell wall and may easily hamper the structural compactness of the *E. coli* cell wall by their sheer large presence in numbers (Fig. 12c). If the structural compactness of the cell is compromised, it becomes permeable to the external atmosphere and hence may suffer death by irreparable damage process (Fig. 12d). Similar mechanisms are suggested in the case of antimicrobial mechanisms of the $\text{Mg}(\text{OH})_2$ nanoparticles [37, 49–51]. As a result, the bacteriostatic effect can happen. Such a picturization matches with the experimentally measured data scenario (Supplementary Fig. S3, Figs. 10 and 11).

However, the relative number of Ca^{2+} ions available per unit reaction area will be dependent on their

original formation process. In other words, it will be dependent on the molarities of the corresponding reactants. Therefore, functional variation in the antimicrobial performance of the samples is expected. The same is also indeed observed from the experimental data (Supplementary Figs. S3, Figs. 10 and 11). The continuance and/or partial or full stoppage of the reaction process will also depend on the actual number of Ca^{2+} ions still available for further adsorption onto the *E. coli* cell walls and the number of unaffected cell walls available. Hence, a time-dependent relative variation in functional antimicrobial performance of the samples is also expected. The same is also reflected in the experimental data (Supplementary Figs. S3, Figs. 10 and 11).

Based on literature reports [38, 42–49], it emerges as a general consensus that the hydroxyl ions (OH^-) play the most major role in the antimicrobial activity of $\text{Ca}(\text{OH})_2$ nanoparticles against *E. coli*. One of the

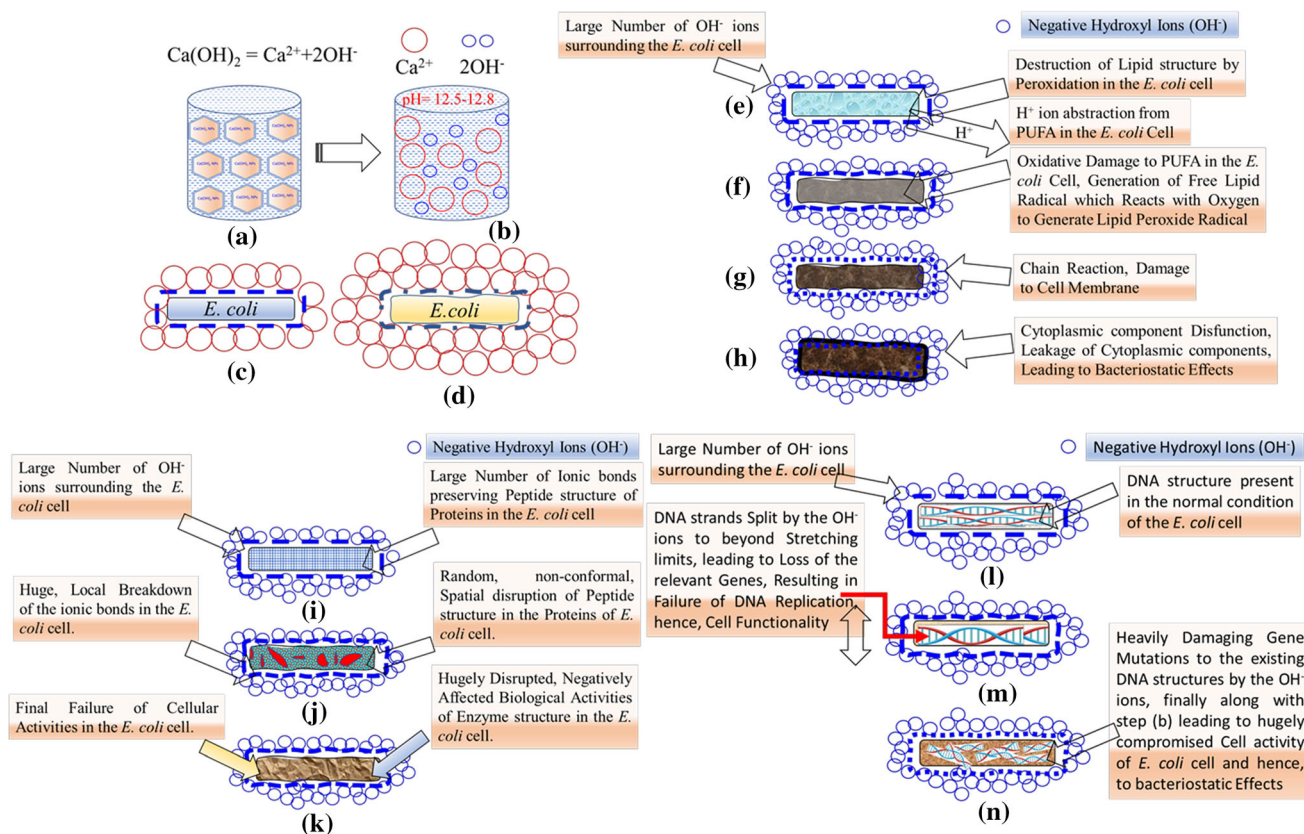


Figure 12 Schematic mechanism of the role of Ca^{2+} in antimicrobial performance: **a** $\text{Ca}(\text{OH})_2$ nanoparticles; **b** dissociation into Ca^{2+} and OH^- ions; **c** accumulation of Ca^{2+} cations on the *E. coli* cell wall; **d** hamper of structural compactness of the *E. coli* cell by cations; Schematic mechanism of the role of the hydroxyl radical (OH^\cdot) in antimicrobial efficacies: **a** formation of hydroxyl radicals, **b** hydroxyl radicals damage the *E. coli* cell wall, **c** DNA structures disruption; schematic mechanism of the

effect of the hydroxyl ions (OH^\cdot) on the cytoplasmic membrane, **e** OH^\cdot ion leads to peroxidation in the *E. coli* cell, **f** generation of lipid peroxide radical, **g** damage of cell membrane, **h** cytoplasmic component dysfunction, **i** peptide structure preserved by ionic bond, **j** local breakdown of the ionic bonds leads to spatial disruption of peptide structure, **k** failure of enzyme activities, **l** DNA structure in *E. coli* cell surrounded by OH^\cdot , **m** stretching of DNA strands, and **n** gene mutation damaged in DNA structure.

major reasons for the antimicrobial activity is of course the very high pH, e.g., 12.5 to 12.8 of the aqueous solution of $\text{Ca}(\text{OH})_2$. Such highly alkaline pH creates a condition that makes it difficult for *E. coli* as well as other microbial agents to completely survive through [38, 42–45].

The pH of control, i.e., nutrient broth (N.B.) + *E. coli* and nutrient broth (N.B.) + *E. coli* + calcium hydroxide, was measured as a function of time, and the data are given in Supplementary Table S1. These data confirm that with an increase in molarity, the pH value increases (Table S1). The pH increase with the increase in molarity has also been reported for basic compounds [50] and is well corroborated with the present study.

It is reported further that with the increase and decrease of pH value from the neutral value of pH 7,

the antibacterial properties enhance [51, 52]. In the present study also, the antibacterial activity was found to be improved with increase in molarity due to an increase in pH as shown in Supplementary Table S1 and the respective antibacterial data shown in Fig. S3. Furthermore, the reduction in pH when N.B. is introduced to *E. coli* (Table S1) is well corroborated with the literature [53, 54]. The decrease in pH value of control (N.B. + *E. coli*) is due to the absorption of glucose by *E. coli*. As mentioned earlier in aqueous solution, $\text{Ca}(\text{OH})_2$ dissociates into one Ca^{2+} ion and two OH^- ions. Obviously, the (OH^-) ions contribute to the high pH values as mentioned above.

Also, it needs to be recognized that per one single (Ca^{2+}) ion, there will be two (OH^-) ions. So, it is obvious that the number of the OH^- ions per unit

area of the interaction front with the *E. coli* cells will be twice as high as the number of (Ca^{2+}) ions. Therefore, the maximum efficacy is expected to come from the roles of the (OH^-) ions as far as the antimicrobial efficacy of the present nano- $\text{Ca}(\text{OH})_2$ particles against the *E. coli* cells is concerned. It is also the general consensus view from literature reports [35, 36, 38–63] that the (OH^-) ions present in the nano-/micro- $\text{Ca}(\text{OH})_2$ materials help to provide the maximum antimicrobial efficacies.

The hydroxyl ions have an effective radius of about 153 pm. Thus, there can be approximately 6.41×10^7 number of the (OH^-) ions on the effective surface of a single *E. coli* cell. This is nearly 2.3 times the number of the Ca^{2+} ions that could be available for interaction with a single *E. coli* cell, as discussed earlier. Therefore, it is obvious that among all the four possible contributors including the (OH^-) ions as discussed above, the (OH^-) ions will provide the maximum contribution to develop antimicrobial efficacy against the *E. coli* cell.

These hydroxyl ions are present a plenty but in different amounts, as shown by the FTIR spectra (Fig. 6) of the present samples S1, S2, S3, and S4. This difference in the relative amounts of the (OH^-) ions also justifies why they exhibit relative differences in their antimicrobial performances against the *E. coli* cells (Supplementary Fig. S3a–d). These OH^- ions are basically free radicals. As a result, they can exhibit very high but indiscriminate reactivity to several materials including biomolecules [20, 35–63]. Thus, there can be three possible ways in which the presence of the OH^- ions can particularly enhance the antimicrobial activities of the $\text{Ca}(\text{OH})_2$ nanoparticles developed in the present work.

For instance, these OH^- ions can cause huge damage to the cytoplasmic membrane that protects the *E. coli* cell as shown schematically in Fig. 12e, f, g, and h [38]. Further, these (OH^-) ions can damage the proteins present in the *E. coli* cell [38, 42] as depicted schematically in Fig. 12i, j, and k. Furthermore, it can cause damage to the DNA present in the cell structure as illustrated schematically in Fig. 12l, m, and n [38, 42–48]. Furthermore, the hydroxyl radicals produced as ROS [20] have enough capacity to damage the *E. coli* cell wall [56]. It can also partially or totally disrupt the DNA structures present in the *E. coli* genome. In addition, the singlet oxygen ($^1\text{O}_2$) species produced as ROS [20] have enough capacity to cause partial or total disruption of the DNA structures

present in the *E. coli* genome [37, 38] and to damage the *E. coli* cell wall by oxidative stress generation [56–63].

Design implications

Especially during the last two decades [1–20], the major new application domains of micro/nano- $\text{Ca}(\text{OH})_2$ are opening up tremendously. To widen it further, there must be means to tune its functional application related properties, e.g., anti-microbial, anti-biofilm-formation, anti-fouling, and heritage conservation, etc. In this context, to the best of the knowledge of the current authors, the total amount of work reported for both synthesis and antimicrobial application of nano- $\text{Ca}(\text{OH})_2$ against a standard bacterium, e.g., *E. coli*, is far from significant [20]. However, the present work possibly for the first time demonstrates that it is possible to tune the microstructure, thermal stability, optical band gap energy, defect structure, and hence the antimicrobial functionality of the nano- $\text{Ca}(\text{OH})_2$ powders over a reasonably wide range.

The design implications of these new findings may result in the development of microstructurally tuned (MT) nano- $\text{Ca}(\text{OH})_2$ for anti-microbial applications against a given bacterium. In other words, the application domains of MT nano- $\text{Ca}(\text{OH})_2$ materials may be further extended to other bacteria and viruses to examine their efficacies. If this stage is successfully achieved, the same materials may be doped with appropriate anti-microbial/anti-viral agents to extend the application zones further against both bacteria and viruses. In other words, the present results highlight the possibilities of being able to tune the functional properties of a given nano- $\text{Ca}(\text{OH})_2$ by varying the synthesis conditions suitably. Such MT nano- $\text{Ca}(\text{OH})_2$ materials may find wide varieties of applications in cosmetics, skin care, and drug industries as well as in various facets of biotechnology-oriented industries.

Conclusions

The present work demonstrates possibly for the very first time that it is possible to tune over a reasonably wide range the microstructure, nanocrystallite size, lattice strain, thermal stability, optical band gap energy, defect structure, and hence, the antimicrobial

functionality of the phase pure nano- $\text{Ca}(\text{OH})_2$ powders against the *E. coli* cells. The microstructurally tuned (MT) phase pure nano- $\text{Ca}(\text{OH})_2$ powders are developed by an inexpensive chemical precipitation technique through the simultaneous variations in molarities of equimolar concentrations (e.g., 0.4, 0.6, 0.8, and 1 M) of both the reactants, e.g., calcium nitrate tetrahydrate ($\text{Ca}(\text{NO}_3)_2 \cdot 4\text{H}_2\text{O}$) as the precursor and NaOH as the precipitant. The MT $\text{Ca}(\text{OH})_2$ materials are characterized by the conventional techniques, e.g., XRD, FESEM, TEM, FTIR, DTA, TGA, UV-Vis spectroscopy, and agar plate well diffusion method. The results obtained from each characterization technique generally correlate nicely with the results obtained from the other characterization techniques. The possible mechanisms of antimicrobial efficacies and relative variations of the same are schematically presented as well as discussed in terms of the relative variations in the amounts of different ROS species, relative variations in their specific activities and relative variations in the number of cations and OH^- ions in the various MT nano- $\text{Ca}(\text{OH})_2$ powders synthesized by appropriate simultaneous variations of molarities of both the precursor and the precipitator solutions. The design implications of the current results in terms of probable futuristic industrial applications are also pointed out. Finally, a hint on possible areas worth of further, dedicated, systematic investigations in the future is provided.

Funding

This work was financially supported through Enhanced Seed Grant Endowment Fund Project No EF/2019–20//QE04-06 provided to the author PK and the Enhanced Seed Grant Endowment Fund Project No. EF/2019–20/QEO4-01 dated 30.04.2019 provided to the author MD by the Directorate of Research at the Manipal University Jaipur (MUJ). It was also financially supported by the Industry Sponsored Project of RI Instruments & Innovation India Ref: RIIMI/PROJ/MUJ/2020 tenable at the Department of Physics, School of Basic Sciences, Faculty of Science, Manipal University Jaipur. It was also supported by the financial support from DST-SERB Imprint Project with sanction no. IMP/2019/000004 dated 16th December 2019 sanctioned to the

author MD. The authors acknowledge the infrastructural supports received from the Central Analytical Facility (CAF) at MUJ for the UV-Vis, FTIR, and DTA-TGA measurements, MRC, MNIT Jaipur for the FESEM and HRTEM measurements and DIAT, Pune, for the XRD measurements.

Declarations

Conflict of interest The authors declare that they have no conflict of interest.

Supplementary Information: The online version contains supplementary material available at <http://doi.org/10.1007/s10853-022-07198-5>.

References

- [1] Komabayashi T, Ahn C, Spears R, Zhu Q (2014) Comparison of particle morphology between commercial- and research-grade calcium hydroxide in endodontics. *J Oral Sci* 56:195–199. <https://doi.org/10.2334/josnurd.56.195>
- [2] Bahman S, Sara G, Somayeh H, Parvin T, Kalhori KAM, Mona S, Reza F (2020) Combined effects of calcium hydroxide and photobiomodulation therapy on apexogenesis of immature permanent teeth in dogs. *J Photochem Photobiol B* 207:111867. <https://doi.org/10.1016/j.jphotobiol.2020.111867>
- [3] Elchaghaby MA, Moheb DM, El Shahawy OI, Abd Alsamad AM, Rashed MAM (2020) Clinical and radiographic evaluation of indirect pulp treatment of young permanent molars using photo-activated oral disinfection versus calcium hydroxide: a randomized controlled pilot trial. *BDJ Open* 6:4–4. <https://doi.org/10.1038/s41405-020-0030-z>
- [4] Thawre S, Joshi R, Bhardwaj SB, Bhushan J (2020) Comparison of the antibacterial efficacy of tea, tree oil, nisin and calcium hydroxide against *Enterococcus faecalis*. *Mater Today Proc* 28:1477–1480. <https://doi.org/10.1016/j.matpr.2020.04.824>
- [5] Afkhami F, Rostami G, Batebi S, Bahador A (2021) Residual antibacterial effects of a mixture of silver nanoparticles/calcium hydroxide and other root canal medicaments against *Enterococcus faecalis*. *J Dent Sci*. <https://doi.org/10.1016/j.jds.2021.11.013>
- [6] Yamanaka S, Hirano S, Uwai K, Tokuraku K (2020) Design of calcium hydroxide-based granules for livestock sanitation. *Case Stud Chem Environ Eng* 2:100005. <https://doi.org/10.1016/j.cscee.2020.100005>
- [7] Natali I, Tempesti P, Carretti E, Potenza M, Sansoni S, Baglioni P, Dei L (2014) Aragonite crystals grown on bones

- by reaction of CO_2 with nanostructured $\text{Ca}(\text{OH})_2$ in the presence of collagen. *Implic Archaeol Paleont Langmuir* 30:660–668. <https://doi.org/10.1021/la404085v>
- [8] Lee H-G, Cho CH, Kim HK, Yoo S (2020) Improved physical and mechanical properties of food packaging films containing calcium hydroxide as a CO_2 adsorbent by stearic acid addition. *Food Packag Shelf Life* 26:100558. <https://doi.org/10.1016/j.fpsl.2020.100558>
- [9] Gollsch M, Afflerbach S, Angadi BV, Linder M (2020) Investigation of calcium hydroxide powder for thermochemical storage modified with nanostructured flow agents. *Sol Energy* 201:810–818. <https://doi.org/10.1016/j.solener.2020.03.033>
- [10] Funayama S, Takasu H, Kim ST, Kato Y (2020) Thermochemical storage performance of a packed bed of calcium hydroxide composite with a silicon-based ceramic honeycomb support. *Energy* 201:117673. <https://doi.org/10.1016/j.energy.2020.117673>
- [11] Lei J, Law WW, Yang E-H (2021) Effect of calcium hydroxide on the alkali-silica reaction of alkali-activated slag mortars activated by sodium hydroxide. *Constr Build Mater* 272:121868. <https://doi.org/10.1016/j.conbuildmat.2020.121868>
- [12] Liang Y (2020) Mechanical and fracture properties of calcium silicate hydrate and calcium hydroxide composite from reactive molecular dynamics simulations. *Chem Phys Lett* 761:138117. <https://doi.org/10.1016/j.cplett.2020.138117>
- [13] Swain SK, Bhattacharyya S, Sarkar D (2015) Fabrication of porous hydroxyapatite scaffold via polyethylene glycol-polyvinyl alcohol hydrogel state. *Mater Res Bull* 64:257–261. <https://doi.org/10.1016/j.materresbull.2014.12.072>
- [14] Granizo ML, Alonso S, Blanco-Varela MT, Palomo A (2002) Alkaline activation of metakaolin: effect of calcium hydroxide in the products of reaction. *J Am Ceram Soc* 85:225–231. <https://doi.org/10.1111/j.1151-2916.2002.tb00070.x>
- [15] Rodriguez-Navarro C, Suzuki A, Ruiz-Agudo E (2013) Alcohol dispersions of calcium hydroxide nanoparticles for stone conservation. *Langmuir* 29:11457–11470. <https://doi.org/10.1021/la4017728>
- [16] López-Arce P, Gomez-Villalba LS, Pinho L, Fernández-Valle ME, de Buergo MÁ, Fort R (2010) Influence of porosity and relative humidity on consolidation of dolostone with calcium hydroxide nanoparticles: effectiveness assessment with non-destructive techniques. *Mater Charact* 61:168–184. <https://doi.org/10.1016/j.matchar.2009.11.007>
- [17] Dei L, Salvadori B (2006) Nanotechnology in cultural heritage conservation: nanometric slaked lime saves architectonic and artistic surfaces from decay. *J Cult Herit* 7:110–115. <https://doi.org/10.1016/j.culher.2006.02.001>
- [18] Ogata F, Kagiya Y, Saenjum C, Nakamura T, Kawasaki N (2020) Performance of poly- γ -glutamic acid–calcium hydroxide treatment for phosphate removal and applicability of the resulting flocculant as a phosphate-based fertilizer. *Bioresour Technol Rep* 11:100464. <https://doi.org/10.1016/j.biteb.2020.100464>
- [19] Antony D, Yadav R, Kalimuthu R, Kumuthan MS (2022) Phyto-complexation of galactomannan-stabilized calcium hydroxide and selenium-calcium hydroxide nanocomposite to enhance the seed-priming effect in *Vigna radiata*. *Int J Biol Macromol* 194:933–944. <https://doi.org/10.1016/j.ijbio.2021.11.148>
- [20] Samanta A, Podder S, Ghosh CK, Bhattacharya M, Ghosh J, Mallik AK, Dey A, Mukhopadhyay AK (2017) ROS mediated high anti-bacterial efficacy of strain tolerant layered phase pure nano-calcium hydroxide. *J Mech Behav Biomed Mater* 72:110–128. <https://doi.org/10.1016/j.jmbbm.2017.04.004>
- [21] Khachani M, El Hamidi A, Halim M, Arsalane S (2014) Non-isothermal kinetic and thermodynamic studies of the dehydroxylation process of synthetic calcium hydroxide $\text{Ca}(\text{OH})_2$. *J Mater Environ Sci* 5:615–624. <https://doi.org/10.1016/j.jmbbm.2017.04.004>
- [22] Schaube F, Koch L, Wörner A, Müller-Steinhagen H (2012) A thermodynamic and kinetic study of the de- and rehydration of $\text{Ca}(\text{OH})_2$ at high H_2O partial pressures for thermochemical heat storage. *Thermochim Acta* 538:9–20. <https://doi.org/10.1016/j.tca.2012.03.003>
- [23] Dutta S, Shirai T (1974) Kinetics of drying and decomposition of calcium hydroxide. *Chem Eng Sci* 29:2000–2003. [https://doi.org/10.1016/0009-2509\(74\)85021-9](https://doi.org/10.1016/0009-2509(74)85021-9)
- [24] Beaudoin JJ, Sato T, Tumidajski PJ (2006) The Thermal decomposition of $\text{Ca}(\text{OH})_2$ polymorphs. In: 2nd International Symposium on Advances in Concrete Through Science and Engineering, RILEM, Québec City, Canada. pp 1–11. <https://nrc-publications.canada.ca/eng/view/accepted/?id=bedec8af-029a-4fe9-96e3-55790cfbb648>
- [25] Bayliss P (1964) Effect of particle size on differential thermal analysis. *Nature* 201:1019–1019. <https://doi.org/10.1038/2011019a0>
- [26] Van Der Marel HW (1956) Quantitative differential thermal analyses of clay and other minerals. *Am Mineral* 41:222–244
- [27] Pishtshev A, Karazhanov S, Klopov M (2014) Materials properties of magnesium and calcium hydroxides from first-principles calculations. *Comput Mater Sci* 95:693–705. <https://doi.org/10.1016/j.commatsci.2014.07.007>
- [28] Wang R, Lang J, Liu Y, Lin Z, Yan X (2015) Ultra-small, size-controlled $\text{Ni}(\text{OH})_2$ nanoparticles: elucidating the

- relationship between particle size and electrochemical performance for advanced energy storage devices. *NPG Asia Mater* 7:e183–e183. <https://doi.org/10.1038/am.2015.42>
- [29] M Singh, A Singhal (2018) Modeling of shape and size effects for the band gap of semiconductor nanoparticles. In: 2018 2nd International Conference on Micro-Electronics and Telecommunication Engineering (ICMETE), IEEE. 339–342. <https://doi.org/10.1109/ICMETE.2018.00080>
- [30] Qi WH, Wang MP, Liu QH (2005) Shape factor of non-spherical nanoparticles. *J Mater Sci* 40:2737–2739. <https://doi.org/10.1007/s10853-005-2119-0>
- [31] Samanta P (2020) Band gap engineering, quantum confinement, defect mediated broadband visible photoluminescence and associated quantum states of size tuned zinc oxide nanostructures. *Optik* 221:165337. <https://doi.org/10.1016/j.ijleo.2020.165337>
- [32] Paul TC, Babu MH, Podder J, Dev BC, Sen SK, Islam S (2021) Influence of Fe^{3+} ions doping on TiO_2 thin films: defect generation, d-d transition and band gap tuning for optoelectronic device applications. *Phys B Condens Matter* 604:412618. <https://doi.org/10.1016/j.physb.2020.412618>
- [33] Das A, Mandal AC, Roy S, Nambissan PMG (2018) Internal defect structure of calcium doped magnesium oxide nanoparticles studied by positron annihilation spectroscopy. *AIP Adv* 8:095013. <https://doi.org/10.1063/1.5001105>
- [34] Liu X, Sui B, Camargo PHC, Wang J, Sun J (2021) Tuning band gap of MnO_2 nanoflowers by Alkali metal doping for enhanced Ferroptosis/phototherapy synergism in Cancer. *Appl Mater Today* 23:101027. <https://doi.org/10.1016/j.apmt.2021.101027>
- [35] Krishnamoorthy K, Moon JY, Hyun HB, Cho SK, Kim S-J (2012) Mechanistic investigation on the toxicity of MgO nanoparticles toward cancer cells. *J Mater Chem* 22:24610–24617. <https://doi.org/10.1039/C2JM35087D>
- [36] Vatsha B, Tetyana P, Shumbula PM, Ngila JC, Sikhwivhilu LM, Moutloali RM (2013) Effects of precipitation temperature on nanoparticle surface area and antibacterial behaviour of $\text{Mg}(\text{OH})_2$ and MgO nanoparticles. *J Biomater Nanobiotechnol* 4:365–373. <https://doi.org/10.4236/jbnb.2013.44046>
- [37] Pan X, Wang Y, Chen Z, Pan D, Cheng Y, Liu Z, Lin Z, Guan X (2013) Investigation of antibacterial activity and related mechanism of a series of nano- $\text{Mg}(\text{OH})_2$. *ACS Appl Mater Interfaces* 5:1137–1142. <https://doi.org/10.1021/am302910q>
- [38] Siqueira JF, Lopes HP (1999) Mechanisms of antimicrobial activity of calcium hydroxide: a critical review. *Int Endod J* 32:361–369. <https://doi.org/10.1046/j.1365-2591.1999.00275.x>
- [39] da Silva BL, Abuçafy MP, Manaia EB, Oshiro Junior JA, Chiari-Andréo BG, Pietro RCR, Chiavacci LA (2019) Relationship between structure and antimicrobial activity of zinc oxide nanoparticles: an overview. *Int J Nanomed* 14:9395–9410. <https://doi.org/10.2147/IJN.S216204>
- [40] Ponnuruvelu DV, Selvaraj A, Suriyraj SP, Selvakumar R, Pulithadathail B (2016) Ultrathin hexagonal MgO nanoflakes coated medical textiles and their enhanced antibacterial activity. *Mater Res Express* 3:105005. <https://doi.org/10.1088/2053-1591/3/10/105005>
- [41] Zhang L, Yin L, Wang C, Lun N, Qi Y (2010) Sol–gel growth of hexagonal faceted ZnO prism quantum dots with polar surfaces for enhanced photocatalytic activity. *ACS Appl Mater Interfaces* 2:1769–1773. <https://doi.org/10.1021/am100274d>
- [42] Delgado RJR, Gasparoto TH, Sipert CR, Pinheiro CR, de Moraes IG, Garcia RB, Duarte MAH, Bramante CM, Torres SA, Garlet GP, Campanelli AP, Bernardineli N (2013) Antimicrobial activity of calcium hydroxide and chlorhexidine on intratubular *Candida albicans*. *Int J Oral Sci* 5:32–36. <https://doi.org/10.1038/ijos.2013.12>
- [43] Ballal V, Kundabala M, Acharya S, Ballal M (2007) Antimicrobial action of calcium hydroxide, chlorhexidine and their combination on endodontic pathogens. *Aust Dent J* 52:118–121. <https://doi.org/10.1111/j.1834-7819.2007.tb00475.x>
- [44] Mohammadi Z, Shalavi S, Yazdizadeh M (2012) Antimicrobial activity of calcium hydroxide in endodontics: a review. *Chonnam Med J* 48:133–140. <https://doi.org/10.4068/cmj.2012.48.3.133>
- [45] Ba-Hattab R, Al-Jamie M, Aldreib H, Alessa L, Alonazi M (2016) Calcium hydroxide in endodontics: an overview. *Open J Stomatol* 6:274–289. <https://doi.org/10.4236/ojst.2016.612033>
- [46] Athanassiadis B, Walsh LJ (2017) Aspects of solvent chemistry for calcium hydroxide medicaments. *Materials* 10:1219. <https://doi.org/10.3390/ma10101219>
- [47] Kim M-A, Rosa V, Neelakantan P, Hwang Y-C, Min K-S (2021) Characterization, antimicrobial effects, and cytocompatibility of a root canal sealer produced by pozzolan reaction between calcium hydroxide and silica. *Materials* 14:2863. <https://doi.org/10.3390/ma14112863>
- [48] Nishanthi VRR (2021) Role of calcium hydroxide in dentistry: a review. *Int J Pharm Res* 12:2822–2827. <https://doi.org/10.31838/ijpr/2020.12.02.377>
- [49] Halbus AF, Horozov TS, Paunov VN (2019) Controlling the antimicrobial action of surface modified magnesium hydroxide nanoparticles. *Biomimetics* 4:41. <https://doi.org/10.3390/biomimetics4020041>

- [50] (2020) Relationship between pH values and molarity of acids and alkalis. <https://www.aplustopper.com/relationship-ph-values-molarity-acids-alkalis/#:~:text=Conclusion%3A,will%20increase%20its%20pH%20value>
- [51] Saliani M, Jalal R, Goharshadi EK (2015) Effects of pH and temperature on antibacterial activity of zinc oxide nanofluid against *Escherichia coli* O157: H7 and *Staphylococcus aureus*. Jundishapur J Microbiol 8:e17115. <https://doi.org/10.5812/jjm.17115>
- [52] ElReash AA, Hamama H, Eldars W, Lingwei G, Zaen El-Din AM, Xiaoli X (2019) Antimicrobial activity and pH measurement of calcium silicate cements versus new bioactive resin composite restorative material. BMC Oral Health 19:235. <https://doi.org/10.1186/s12903-019-0933-z>
- [53] Fernández RO, Antón DN (1987) Bacteriostatic action of streptomycin on ribosomally resistant mutants (rpsL) of *Salmonella typhimurium*. Antimicrob Agents Chemother 31:1627–1631
- [54] Sánchez-Clemente R, Igeño MI, Población AG, Guijo MI, Merchán F, Blasco R (2018) Study of pH changes in media during bacterial growth of several environmental strains. Proceedings 2:1297. <https://doi.org/10.3390/proceedings2201297>
- [55] Boudreau MA, Fisher JF, Mobashery S (2012) Messenger functions of the bacterial cell wall-derived muropeptides. Biochemistry 51:2974–2990. <https://doi.org/10.1021/bi300174x>
- [56] Li Y, Zhang W, Niu J, Chen Y (2012) Mechanism of photogenerated reactive oxygen species and correlation with the antibacterial properties of engineered metal-oxide nanoparticles. ACS Nano 6:5164–5173. <https://doi.org/10.1021/nn300934k>
- [57] Prasanna VL, Vijayaraghavan R (2015) Insight into the mechanism of antibacterial activity of ZnO: surface defects mediated reactive oxygen species even in the dark. Langmuir 31:9155–9162. <https://doi.org/10.1021/acs.langmuir.5b02266>
- [58] Vatansever F, de Melo WCMA, Avci P, Vecchio D, Sadasiyam M, Gupta A, Chandran R, Karimi M, Parizotto NA, Yin R, Teges GP, Hamblin MR (2013) Antimicrobial strategies centered around reactive oxygen species–bactericidal antibiotics, photodynamic therapy, and beyond. FEMS Microbiol Rev 37:955–989. <https://doi.org/10.1111/1574-6976.12026>
- [59] Halliwell B, Gutteridge JMC (2015) Free radicals in biology and medicine, 5th edn. Oxford University Press, Oxford
- [60] Godoy-Gallardo M, Eckhard U, Delgado LM, de Roo Puente YJD, Hoyos-Nogués M, Gil FJ, Perez RA (2021) Antibacterial approaches in tissue engineering using metal ions and nanoparticles: from mechanisms to applications. Bioact Mater 6:4470–4490. <https://doi.org/10.1016/j.bioactmat.2021.04.033>
- [61] Wang E, Huang Y, Du Q, Sun Y (2017) Silver nanoparticle induced toxicity to human sperm by increasing ROS(reactive oxygen species) production and DNA damage. Environ Toxicol Pharmacol 52:193–199. <https://doi.org/10.1016/j.eta.2017.04.010>
- [62] de Lucca Camargo L, Touyz RM (2019) Reactive oxygen species. In: Touyz RM, Delles C (eds) Textbook of vascular medicine. Springer International Publishing, Cham, pp 127–136
- [63] Kwak MS, Rhee WJ, Lee YJ, Kim HS, Kim YH, Kwon MK, Shin J-S (2021) Reactive oxygen species induce Cys106-mediated anti-parallel HMGB1 dimerization that protects against DNA damage. Redox Biol 40:101858. <https://doi.org/10.1016/j.redox.2021.101858>

Publisher's Note Springer Nature remains neutral with regard to jurisdictional claims in published maps and institutional affiliations.